INTERNATIONAL JOURNAL OF
NUMERICAL ANALYSIS AND MODELING
Volume 19, Number 6, Pages 777–792

ASYMPTOTIC AND EXACT SELF-SIMILAR EVOLUTION OF A GROWING DENDRITE

AMLAN K. BARUA, SHUWANG LI, XIAOFAN LI, AND PERRY LEO

Abstract. In this paper, we investigate numerically the *long-time* dynamics of a two-dimensional dendritic precipitate. We focus our study on the self-similar scaling behavior of the primary dendritic arm with profile $x \sim t^{\alpha_1}$ and $y \sim t^{\alpha_2}$, and explore the dependence of parameters α_1 and α_2 on applied driving forces of the system (e.g. applied far-field flux or strain). We consider two dendrite forming mechanisms: the dendritic growth driven by (i) an anisotropic surface tension and (ii) an applied strain at the far-field of the elastic matrix. We perform simulations using a spectrally accurate boundary integral method, together with a rescaling scheme to speed up the intrinsically slow evolution of the precipitate. The method enables us to accurately compute the dynamics far longer times than could previously be accomplished. Comparing with the original work on the scaling behavior $\alpha_1 = 0.6$ and $\alpha_2 = 0.4$ [Phys. Rev. Lett. 71(21) (1993) 3461–3464], where a constant flux was used in a diffusion only problem, we found at long times this scaling still serves a good estimation of the dynamics though it deviates from the asymptotic predictions due to slow retreats of the dendrite tip at later times. In particular, we find numerically that the tip grows self-similarly with $\alpha_1 = 1/3$ and $\alpha_2 = 1/3$ if the driving flux $J \sim 1/R(t)$ where $R(t)$ is the equivalent size of the evolving precipitate. In the diffusive growth of precipitates in an elastic media, we examine the tip of the precipitate under elastic stress, under both isotropic and anisotropic surface tension, and find that the tip also follows a scaling law.

Key words. Moving boundary problems, self-similar, dendrite growth, boundary integral equations.

1. Introduction

The evolution of precipitates during a solid-solid phase transformation is a classical example for studying interface dynamics or systems driven out of equilibrium. A well-known feature observed during the phase transformation is the formation of various dendritic microstructures, depending on the physical conditions (e.g. the composition of the phases, the interfacial crystallographic properties and the applied far-field flux). Usually a dendrite includes the primary arm (tip region) and accompanied side-branches. One key aspect of studying the precipitate morphology is to understand the evolution of tip profile, as its dynamics determines the resulting morphology of the dendrite.

An early theory trying to describe the dendritic tip is due to Ivantsov [4] who assumed that the region near the tip of a dendrite is a branch-less paraboloid growing with a constant velocity. These assumptions allow him to solve the steady state heat transport equation and establish an analytical relation between the Stefan number and the Peclet number, the two dimensionless quantities important for the process. A large number of work was built upon this original formulation. For example, capillary effects were coupled to heat transfer problem through Gibbs-Thomson condition due to the work of Nash and Glicksmann [21, 22]. In a more recent paper [19], Lacombe et. al. showed that paraboloid shape assumption was not valid if one moves slightly away from the tip and to a region where the side

Received by the editors February 27, 2022 and, in revised form, June 2, 2022; accepted June 19, 2022.

2000 *Mathematics Subject Classification.* 52B10, 65D18, 68U05, 68U07.

branches emanate. They showed that a much better match with experiments occurs if a fourth-order correction, in terms of radius of curvature of the tip, is applied to the predictions of Ivantsov. Ivantsov's original formulation did not take into account the effects of side-branching, however considerable research has been done in this area where the main question is to understand the frequency and and amplitude of the secondary branches. These questions are tackled roughly through two approaches. A few authors suggest that the deterministic oscillation at the tip is responsible for side-branching [6, 15, 23]. Others explain the mechanism via stochastic approach and consider selective, thermal fluctuation induced noise to be responsible for side-branching process [2, 5, 8, 10, 14, 16].

Li and Beckerman [1] studied the scaling behavior of both the tip and side branches with different geometric parameters by performing micro-gravity experiments using pure succonitrile crystals. Their experimental results were in good agreement with the theoretical predictions of [2]. A more recent work on dendrite morphology using boundary integral methods can be found in [20, 27] where deterministic side-branching mechanism for 2D and 3D growths were considered.

A seemingly different problem, the Hele-Shaw flow, should also be mentioned in this context. Although the origins of the Hele-Shaw problem lie in creeping flow between two closely placed parallel plates, the flow is governed by similar equations. Interesting results that emerge in a Hele-Shaw cell can be found in [9] where the author investigated formation of different patterns of a growing bubble both in isotropic and anisotropic surface tension. Numerically, the boundary integral method has been the most successful approach in Hele-Shaw flow where long dynamics, both in growing and shrinking interfaces, has been tracked with highly accurate computation in references such as [26,28,29]. Almgren et al. [30] used ideas from selection theory to argue that $\kappa^2 V$, where κ is the tip curvature and V is the tip velocity, should be time independent for a Hele-Shaw bubble. They assumed that a precipitate in its later phase of growth assumes a cross like shape where one can ignore the lateral width of the arms of the precipitate in comparison to the arm-length. From these considerations they derived a scaling law $(x, y) \to (x/t^{\alpha_1}, y/t^{\alpha_2})$ for the growing tip, where t is the elapsed time and α_1 and α_2 are parameters. The sum $\alpha_1+\alpha_2$ depends on the flux J of the incoming material. For constant flux $J = c$ they found these constants to be $\alpha_1 = 0.60$ and $\alpha_2 = 0.40$. Their simulations with moderate and high anisotropy using boundary integral formulation indeed showed the scaling to be true, however they investigated the precipitate growth for a very short time duration. The scaling law was verified experimentally by Ignes-Mullol et al. [17] and very good agreement between the simulation and experiment was observed. In fact their experimentally verified exponent α_1 turned out to be 0.64 which is just slightly off from the theoretical predictions of [30].

In this paper, we expanded the original work of Almgren et al. [30] by answering several interesting questions that emerge naturally from their work. These are: (i) whether the scaling law is valid at long times; (ii) what could be a scaling law for the tip of a precipitate growing under time dependent flux and finally (iii) what happens when precipitate grows in presence elastic fields, i.e. whether the tip still exhibits scaling behavior? Our numerical results suggest that at long times, the Almgren's scaling law still provides a good estimate of the tip-profile although it deviates from the asymptotic predictions due to slow retreat of the dendrite tip at later times. In particular, we find that the tip grows self-similarly with $\alpha_1 = 1/3$ and $\alpha_2 = 1/3$ if the driving flux $J \sim 1/R$ where R is the equivalent radius of the precipitate size. In the diffusive growth of precipitates, we observe the tip of

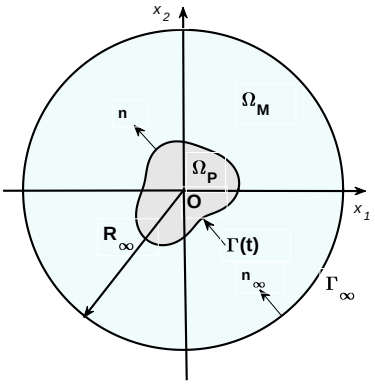

FIGURE 1. Two phase domain with one precipitate occupying the region Ω_P (gray color). The diffusion occurs in the matrix region Ω_M (in cyan) bounded by the moving interface $\Gamma(t)$ and a fixed circular far-field boundary Γ_∞ with large enough radius R_∞. Here, a point with coordinate $\mathbf{x} = (x_1, x_2)$, following the classical elasticity notation, takes the same meaning as the usual $\mathbf{x} = (x, y)$ description.

the precipitate under elastic stress, under both isotropic and anisotropic surface tension, follows a scaling law albeit different from Almgren's.

The paper is organized as follows: the problem formulation and numerical methods are described in Section 2, the numerical results are presented in Section 3, and the future direction of the study is discussed in Section 4.

2. Problem formulation

2.1. Diffusion Problem. We first describe the phase transformation problem. As shown in Fig. 1, the precipitate phase occupies a bounded region Ω_P in the two dimensional plane. The diffusion occurs in the matrix region exterior to the precipitate, where the concentration $U(\mathbf{x}, t)$ of the diffusing species satisfies the Laplace equation under the quasi-static assumption

$$\Delta U = 0, \quad \text{for } \mathbf{x} \in \Omega_M. \tag{1}$$

The boundary condition at the precipitate-matrix interface $\Gamma(t)$ is given by a generalized Gibbs-Thomson condition [7], i.e.,

$$U = \tau_0(1 - \epsilon \cos m\theta)\kappa(\mathbf{x}, t) + ZG_{el}(\mathbf{x}, t), \quad \text{for } \mathbf{x} \in \Gamma(t), \tag{2}$$

where θ is the tangent angle, τ_0 is the surface tension parameter, ϵ is the strength of anisotropy, m is the symmetry mode of anisotropy, $\kappa(\mathbf{x}, t)$ is the local curvature of the interface, $G_{el}(\mathbf{x}, t)$ is the elastic energy, and parameter Z specifies the relative importance between elastic and surface energy. Thus $Z = 0$ implies a pure diffusion case without elastic effects.

At the far-field boundary Γ_∞, we consider a material flux condition

$$J(t) = -\frac{1}{2\pi} \int_{\Gamma_\infty} \nabla U \cdot \mathbf{n}_\infty \, ds, \tag{3}$$

where s indicates arclength, i.e., $ds = \sqrt{(dx)^2 + (dy)^2}$ for (x, y) on a curve, and $J(t)$ is the flux of the diffusing species entering the system across Γ_∞. The flux $J(t)$ is taken to be positive for growth condition and zero for equilibration.

Let $V(\mathbf{x}, t)$ be the velocity of the moving interface. Once the concentration $U(\mathbf{x}, t)$ of the diffusing species in the matrix phase is solved, the velocity of the interface can be computed via

$$V = (\nabla U \cdot \mathbf{n})_{\Gamma(t)}. \tag{4}$$

The equations (1–4) remain virtually unchanged in the case of Hele-Shaw bubble formation, one has to just ignore the term ZG_{el} in Eq. (2) and interpret U as negative of the non-dimensional pressure in the fluid.

2.2. Elasticity Problem. The elastic energy G_{el} is given by the formula

$$G_{el} = \frac{1}{2}\sigma_{ij}^P(\varepsilon_{ij}^P - \varepsilon_{ij}^T) - \frac{1}{2}\sigma_{ij}^M\varepsilon_{ij}^M + \sigma_{ij}^M(\varepsilon_{ij}^M - \varepsilon_{ij}^P), \tag{5}$$

where ε_{ij} and $\sigma_{ij}, i, j = 1, 2$ are the elements of strain and stress tensors either in the matrix phase (superscript "M") or in the precipitate phase (superscript "P"). Also ε_{ij}^T (superscript "T") indicates the transformation (misfit) strain of the precipitates due to unmatched crystal lattice. We also denote the displacement in the matrix and precipitate phase by u^M and u^P, respectively. The elastic energy can be computed once the equations of isotropic elasticity in both matrix and precipitate phase are solved. These elasticity equations read

$$\sigma_{ij,j}^\chi = 0 \quad \text{in } \Omega_\chi \text{ (force balance equation with no body force)} \tag{6}$$

$$u_i^P = u_i^M \quad \text{(continuity of displacement at interface } \Gamma) \tag{7}$$

$$\sigma_{ij}^P n_j = \sigma_{ij}^M n_j \quad \text{(continuity of traction at interface } \Gamma) \tag{8}$$

$$\lim_{r \to R_\infty} \varepsilon_{ij}^M = \varepsilon_{ij}^0 \quad \text{(far-field boundary condition)}, \tag{9}$$

where the superscript or subscript χ can be either "M" or "P" depending on the region where the equation is being applied, and r is the radial distance from the origin. In above equations, we have used the double index notation and Einstein summation convention when solving the elasticity problem in both phases. The relation between the displacement and the strain is given by $\varepsilon_{ij}^\chi = \frac{1}{2}\left(\frac{\partial u_i^\chi}{\partial x_j} + \frac{\partial u_j^\chi}{\partial x_i}\right)$, whereas that between various stresses and strains are given by

$$\sigma_{ij}^P = C_{ijkl}^P\left(\varepsilon_{kl}^P - \varepsilon_{kl}^T\right), \tag{10}$$

$$\sigma_{ij}^M = C_{ijkl}^M\varepsilon_{kl}^M, \tag{11}$$

where the stiffness tensor $C_{ijkl}^\chi = 2\mu^\chi\left[\frac{\nu^\chi}{1-\nu^\chi}\delta_{kl}\delta_{ij} + \delta_{ik}\delta_{jl}\right]$, μ^χ is the shear modulus, ν^χ is the Poisson ratio, and δ_{ij} is the Kronecker delta. The elasticity problem is non-homogeneous - the precipitate and matrix can be two different materials. More about the origin of these equations can be found in [13]

2.3. Boundary integral equations. Both the diffusion and elasticity problem are solved by recasting the original differential equations into boundary integral equations [3, 13]. The integral formulation reduces the original two-dimensional problem to a one dimensional problem defined only at the interface between the precipitate and matrix.

The boundary integral formulation of the elasticity problem is based on the fundamental solution (Kelvin's solution) to the elasticity equations. The displacement and traction components of the fundamental solution are respectively given by

$$U_{jk}(\mathbf{x},\mathbf{x}') = \frac{1}{8\pi\mu\,(1-\nu)}\left[(3-4\nu)\log\left(\frac{1}{r}\right)\delta_{ij} + r_{,j'}r_{,k'}\right],$$
$$T_{jk}(\mathbf{x},\mathbf{x}') = \frac{-1}{4\pi\,(1-\nu)\,r}\left[\frac{\partial r}{\partial \mathbf{n}'}\left((1-2\nu)\,\delta_{jk} + 2r_{,j'}r_{,k'}\right) + (1-2\nu)\left(n'_j r_{,k'} - n'_k r_{,j'}\right)\right],$$

where $r = |\mathbf{x}-\mathbf{x}'|$ is the radial distance between points $\mathbf{x}$ and $\mathbf{x}'$, $r_{,j'} = \frac{\partial r}{\partial x'_j}$, n'_k is the kth component of the unit normal vector $\mathbf{n}'$ at $\mathbf{x}' \in \Gamma(t)$.

The fundamental solution allows us to reformulate the elasticity problem in the precipitate and matrix phase using the following integral equations

$$\frac{1}{2}u_j^P + \int_\Gamma u_k^P T_{jk}^P ds' - \int_\Gamma t_k^P U_{jk}^P ds' = \int_\Gamma t_k^T U_{jk}^P ds', \tag{12}$$
$$\frac{1}{2}u_j^M - \int_\Gamma u_k^M T_{jk}^M ds' + \int_\Gamma t_k^M U_{jk}^M ds' = \frac{1}{2}u_j^0 - \int_\Gamma u_k^0 T_{jk}^M ds' + \int_\Gamma t_k^0 U_{jk}^M ds', \tag{13}$$

where ds' means $ds(\mathbf{x}')$ at the integration point $\mathbf{x}' \in \Gamma(t)$. In these equations u_j, t_k are the unknown displacement and traction defined at point $\mathbf{x} \in \Gamma(t)$. At the interface between matrix and precipitate, we consider a continuity condition $u_i^M = u_i^P$ and $t_k^M = t_k^P$, therefore we drop the superscripts and obtain the final set of equations for the elasticity problem on the matrix-precipitate interface Γ as follows:

$$\frac{1}{2}u_j + \int_\Gamma u_k T_{jk}^P ds' - \int_\Gamma t_k U_{jk}^P ds' = \int_\Gamma t_k^T U_{jk}^P ds', \tag{14}$$
$$\frac{1}{2}u_j - \int_\Gamma u_k T_{jk}^M ds' + \int_\Gamma t_k U_{jk}^M ds' = \frac{1}{2}u_j^0 - \int_\Gamma u_k^0 T_{jk}^M ds' + \int_\Gamma t_k^0 U_{jk}^M ds'. \tag{15}$$

The diffusion problem (or the Hele-Shaw problem) can also be rewritten into an integral equation using a dipole density function ϕ on $\Gamma(t)$,

$$\left(-\frac{1}{2}I + K\right)[\phi] + J\log|\mathbf{x}| = \kappa + ZG_{el}, \tag{16}$$

where I is the identity operator, and K is the integral operator defined as

$$K[\phi](s,t) = \frac{1}{2\pi}\int_{\Gamma(t)} \phi(s',t)\left[\frac{\partial}{\partial \mathbf{n}(s',t)}\log|\mathbf{x}(s',t)-\mathbf{x}(s,t)| + 1\right] ds'. \tag{17}$$

Here, $\mathbf{n}(s',t)$ is the unit normal at the integration point $\mathbf{x}'(s,t)$. Equations (14), (15) and (16) constitute the complete boundary integral formulation of the combined diffusion and elasticity problem. After the diffusion problem is solved, the normal velocity V of the interface is computed using the Dirichlet-Neumann map,

$$V(s,t) = \frac{1}{2\pi}\int_\Gamma \phi_{s'}\frac{\partial}{\partial s}\log|\mathbf{x}(s',t)-\mathbf{x}(s,t)|\,ds' + J(t)\frac{\mathbf{x}(s,t)\cdot\mathbf{n}}{|\mathbf{x}(s,t)|^2}, \tag{18}$$

where $\phi_{s'} = \dfrac{\partial\phi(s',t)}{\partial s'}$. Note that some integrals in Eqs. (14), (15), (16), and (18) are interpreted as principal value integrals due to the logarithmic and Cauchy singularities, when both $\mathbf{x}(s,t), \mathbf{x}(s',t) \in \Gamma(t)$.

2.4. Rescaling scheme. To increase the computational efficiency, we implement a space-time rescaling of the integral equations [11,26] which enables us to compute the evolution of the interface exponentially fast. In this rescaling scheme, the original spatial coordinates $\mathbf{x} = (x, y)$ and time variable t are mapped onto another set of coordinates $\bar{\mathbf{x}} = (\bar{x}, \bar{y})$ and $\bar{t}$. The spatial coordinates of the original and transformed systems are connected by the relation

$$\mathbf{x} = \bar{R}(\bar{t})\,\bar{\mathbf{x}}, \tag{19}$$

where the scale factor of the spatial coordinates $\bar{R}$ is a function of the rescaled time $\bar{t}$. The variables t and $\bar{t}$ are related through the following equation

$$\bar{t} = \int_0^t \frac{1}{f(s)} ds, \tag{20}$$

where f is a positive, continuous function of time t that represents the temporal rescaling. The velocity in the rescaled coordinates therefore becomes

$$V = \frac{d}{dt}\mathbf{x}\cdot\mathbf{n} = \left(\bar{R}(\bar{t})\frac{d\bar{\mathbf{x}}}{d\bar{t}} + \bar{\mathbf{x}}\frac{d\bar{R}}{d\bar{t}}\right)\frac{d\bar{t}}{dt}\cdot\bar{\mathbf{n}}. \tag{21}$$

We define the normal velocity in the rescaled frame $\bar{V} = \dfrac{d\bar{\mathbf{x}}}{d\bar{t}}\cdot\bar{\mathbf{n}}$ and the area $\bar{A} = \dfrac{1}{2}\displaystyle\int_{\bar{\Gamma}} \bar{\mathbf{x}}\cdot\bar{\mathbf{n}}$. Then the flux J in new coordinates becomes

$$J = \frac{1}{2\pi}\int_\Gamma V ds = \frac{1}{2\pi}\int_{\bar{\Gamma}} \bar{R}^2\frac{d\bar{t}}{dt}\bar{V}d\bar{s} + \frac{1}{\pi}\bar{R}\frac{d\bar{R}}{d\bar{t}}\frac{d\bar{t}}{dt}\bar{A}. \tag{22}$$

If we impose the area conservation constraint $\int_{\bar{\Gamma}} \bar{V}d\bar{s} = 0$, then because of Eq. (20), we obtain the equation connecting the spatial and temporal scaling factors as

$$J = \frac{1}{\pi}\frac{\bar{A}\bar{R}}{f(\bar{t})}\frac{d\bar{R}}{d\bar{t}}. \tag{23}$$

For different flux J, we can choose $f(\bar{t})$ such that the spatial scaling factor in Eq. (19) becomes an exponential function of $\bar{t}$. For example, if the flux $J = C$ where C is a constant, we may choose $f(\bar{t}) = \frac{1}{\bar{R}^2}$ whereas if $J = C/\bar{R}$ then we can choose $f(\bar{t}) = \frac{1}{\bar{R}^3}$. Under such conditions we can use Eq. (20) to map the rescaled time $\bar{t}$ to time t using exponential functions, thus a small advancement in the rescaled frame amounts to a large step forward in the actual time. The integral equations of the elasticity and diffusion equations are rescaled accordingly and the details of the formulation can be found in [11]. Note that we do not change the real physics by implementing the rescaling idea.

2.5. Interface dynamics. The explicit methods for updating the interface result in numerical stiffness requiring the time step $\Delta t \sim \mathcal{O}\left(\Delta s^3\right)$, where Δs is arclength spacing of the points on interface. To remove the stiffness, we implement the small scale decomposition technique [18]. This special temporal scheme reduces the stability constraint to $\Delta t \sim \mathcal{O}(\Delta s)$. Following [18], instead of the coordinates of the marker points, we first repose the motion of the interface using the length L of the interface and the tangent angle θ (an angle that the tangent line at the marker point makes with positive x axis). These two quantities evolve according

to the following equations:

$$\bar{L}_t = \int_0^{2\pi} \bar{\theta}_\alpha \bar{V}(\alpha, t) d\alpha, \tag{24}$$

$$\bar{\theta}_t = \frac{2\pi}{\bar{L}} \left(-\bar{V}_\alpha + \bar{T}\bar{\theta}_\alpha \right), \tag{25}$$

where the tangential velocity $\bar{T}$ is obtain by

$$\bar{T}(\alpha, \bar{t}) = \bar{T}(0, \bar{t}) - \int_0^\alpha \bar{s}_\beta \bar{\kappa} \bar{V} d\beta + \frac{\alpha}{2\pi} \int_0^{2\pi} \bar{s}_\beta \bar{\kappa} \bar{V} d\beta. \tag{26}$$

The stiffness of the original problem propagates to Eq. (25) above. We then identify, in the Fourier space, the dominant term on the right-hand side of the Eq. (25) as $-\tau_0 n^3 \theta_n$, where n is the frequency number. We time-integrate the θ-equation in this form with a semi-implicit time stepping algorithm using an integrating factor for dominant term for all values of τ_0. As only the mean value term τ_0 enters the dominant factor, results are more accurate for the cases of small anisotropy. We note that strong anisotropy might not be captured accurately through this, nevertheless, we do this for large anisotropy and observe convergence behavior too. Throughout the calculation, the points are spaced equally in arc-length. At time $t = 0$ this condition is ensured by problem setup. At later time instants this is achieved by adding the tangential velocity, given by Eq. (26), to the marker points [18]. Note that the rescaling does not change the equations of elasticity and they can be solved without any modifications [11, 26].

2.6. Numerical methods. We implement the space-time rescaling, outlined above, in our formulation. We first solve integral equations (14) and (15) to compute G_{el} term for the diffusion problem. We then solve the diffusion problem Eq. (16) and compute the velocity of the interface by Dirichlet-Neumann map [3]. Once the velocity is known, we update the interface following Eq. (24) and (25) via small scale decomposition [18]. Note that the kernels of the integral equations contain logarithmic and Cauchy type singularities and the equations are discretized by spectrally accurate quadratures [13]. The discretized system is solved by an iterative technique, the GMRES (Generalized Minimal Residual) method, with a fast summation algorithm [12]. The fast summation method reduces the computational complexity of GMRES from $\mathcal{O}\left(N^2\right)$ to $\mathcal{O}\left(N \log N\right)$. The details of the computation steps are given in Algorithm 1.

3. Results

The use of the space-time rescaled algorithm enables us to compute the evolution of the precipitate for a very long time with high accuracy. The correctness of these implementations was checked in a number of ways. This includes resolution studies by halving the time step successively to confirm the expected 2nd order temporal convergence, and by doubling the mesh points on the interface to confirm the expected spectral accuracy in space. Our main goal is to simulate the growth of the precipitate under different flux conditions, i.e., constant or variable in time. The tip profile is examined under the scaling law proposed by Almgren et al. [30]. We are interested to verify (i) if the scaling law of [30] about the asymptotic shape holds at a time much longer than that observed in [30], (ii) if there is an asymptotic shape to which the precipitate tip converges under *time varying flux*, and (iii) whether the addition of elastic field preserves self-similarity of the tip under the same scaling law.

Algorithm 1 Numerical algorithm for computing the evolution of the precipitate

Input: Initial shape $\bar{\mathbf{x}}(s,0)$
At $t=0$ perform equal arclength discretization
for $t=0$ to t_{final} **do**
    Discretize the boundary integral equations of the elasticity problem, Eqs. (14) and (15), using alternating point quadrature
    Solve the discrete system for $\bar{u}_j$ and $\bar{t}_k$ using preconditioned GMRES [13]
    Compute $\bar{G}_{el}$ from Eq. (5)
    Discretize the rescaled version [11] of Eq. (16) using alternating point quadrature
    Solve discrete system for $\bar{\phi}$ using preconditioned GMRES [13]
    Compute the normal velocity $\bar{V}$ from Eq. (22)
    Compute the tangential velocity $\bar{T}$ from Eq. (26)
    Update the interface $\bar{\Gamma}(\bar{t})$ using Eq. (24) and (25),
end for

3.1. Asymptotic shape of a precipitate under four fold anisotropic surface tension. In Fig. 2a and 2b, we display the results of a very long time simulation of the precipitate subject to a constant flux $J=1$ and anisotropic surface tension $\tau_0(1-0.0067\cos 4\theta)$. We start our simulation with $N=8192$ marker points on a circular interface $r=1$ and our initial time step was $\Delta t = 6.25\times 10^{-6}$. We use small time steps to compute the movement of the tip with high accuracy. Time step is halved when the space resolution is doubled to maintain the stability constraint.

In Fig. 2b we display the interfaces of the precipitate at different times, we stop the simulation at $t\approx 2956$. We would like to point out that the similar computation in [30] was run only up to time $t=3.5$. Thus our simulation ran more than 800 times longer. During this period, the side arms of the precipitate in our computation grew 50 times more as compared to that of Almgren's simulation. Other things that we wish to stress about this simulation are (i) the suppression of the higher Fourier modes ($>$ 4th mode), which were visible in the initial phase of the precipitate development and (ii) the better match of the shapes at later times with the asymptotic prediction.

In Fig. 2a we have compared the interfaces obtained from our simulations with the asymptotic shape predicted by Almgren et al. [30] assuming complementary power law scaling for x and y axes. At the time when we stop simulation, the x coordinate of the tip of the computed interface is around 1.875 whereas asymptotic predictions of [30] suggests the tip length to be 1.83. Lastly we wish to emphasize that the results in Almgren's paper was obtained on the basis of an intermediate shape of the precipitate, however our results are based on a much later shape which looks significantly different from the shape at early stages of evolution and which is more closer to asymptotic predictions confirming the validity of the theory outlined in [30].

A similar computation is performed for the case of stronger anisotropy with $\epsilon = 0.033$ and other parameters are unchanged. The results of the simulation are displayed in Fig. 3a and Fig. 3b. The simulation is performed up to time $t=200$. After this time, it is difficult to continue with the simulation because of the formation of sharp tips due to the applied strong anisotropy. We observe deviations from four-fold symmetry and have to stop the simulation.

Importantly, the long time evolution of the precipitate displays non-convergence to the asymptotic shape predicted in [30]. While the numerically simulated shape

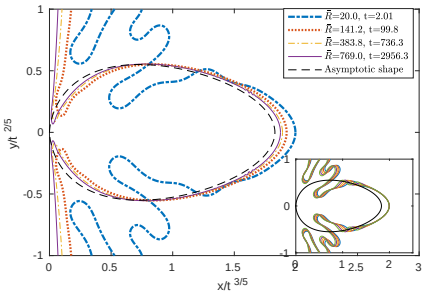

(a) Comparison of numerically computed shape and asymptotic predictions. Inset: Early time stage comparison made by Almgren et al. [30].

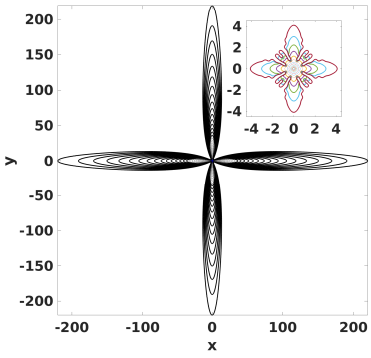

(b) Morphology of the precipitate

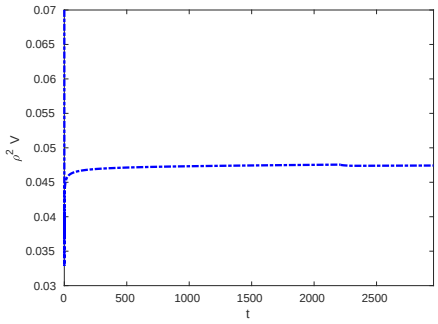

(c) Evolution of $\rho^2 V$ with time

FIGURE 2. Comparison of the shape obtained from nonlinear boundary integral method and the asymptotic shape, Fig. (3) of [30]. The interface is evolving with flux $J = 1$, the initial shape $r = 1$ and $\epsilon = 0.0067$. The asymptotic tip is given in black dotted lines in (a). The scaling specified by [30] works well in this case. As time progresses the tip obtained from simulation gets closer to the asymptotic prediction. In (b) we plot the shape of the precipitate at different times and in (c) we plot the product of $\rho^2 V$ where $\rho = \dfrac{1}{\kappa}, \kappa$ is the curvature and V is the tip velocity. According to [30], as time progresses this should tend to a constant.

match the asymptotic shape around time $t \approx 1.5$, at later times it does not. At the beginning, the length of scaled tip is longer than the asymptotically predicted value of 2.70. But the length of the (scaled) arm shortens as time progresses and tip moves from right to left eventually crossing 2.70. Therefore this is a case where we find disagreement between the theory and simulation.

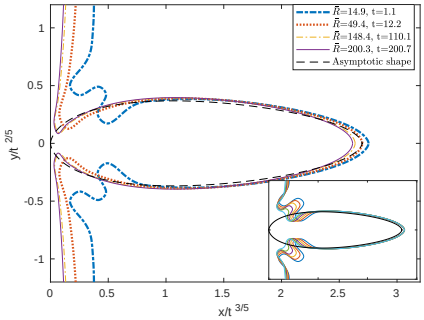

(a) Comparison of numerical results and asymptotic prediction. Inset: Early time stage comparison made by Almgren et al. [30].

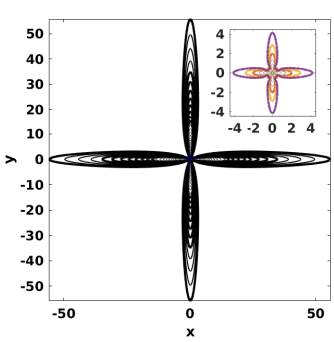

(b) Morphology of the precipitate

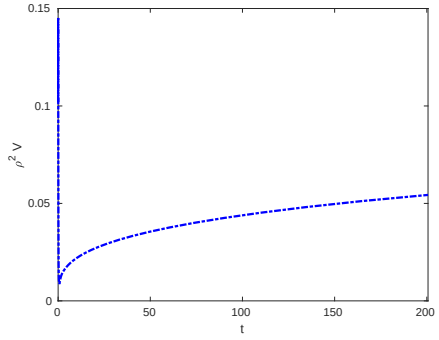

(c) Evolution of $\rho^2 V$ with time

FIGURE 3. Comparison of the shape obtained from nonlinear boundary integral method and the asymptotic shape, Fig. (4) of [30]. In this case, $\epsilon = 0.033$ and remaining parameters are same as that in Fig. (2). The asymptotic tip is given in black dotted line in (a). The scaling specified by [30] not working in this case. In fact the tip computed by the code is initially to the right of the asymptotic tip but it keeps on receding to the left and eventually crosses the asymptotic shape. In (b) we plot the shape of the as time progresses and in (c) we observe that the product of $\rho^2 V$ is not quite constant.

3.2. Simulation results with time increasing flux $J \sim t$. In Fig. 4 we show the simulation result with time varying flux where the flux J grows linearly with time, $J \sim t$ and small anisotropy $\epsilon = 0.0067$. We observe that the increasing flux induces favorable growth condition for more modes as compared to the case of constant flux. For example the 8th mode grows and manifests itself in the form of a small branch between any two adjacent principal arms. Also unlike the case of constant flux, this branch does not vanish.

Scaling behavior: It is not difficult to derive a scaling law for the self-similar growth of a precipitate driven by a flux $J \sim t$. We assume all the conditions that Almgren et al. [30] used in their derivation and take it a step further by considering the relation

$$\frac{dA}{dt} = J(t) \tag{27}$$

between the rate of change of area A of the precipitate and flux.

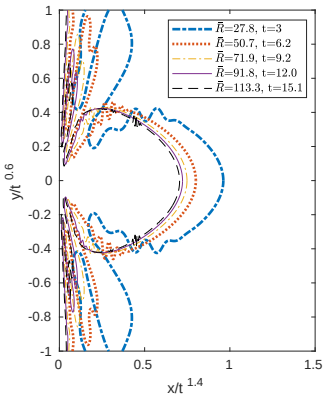

(a) Tip profile of the precipitate

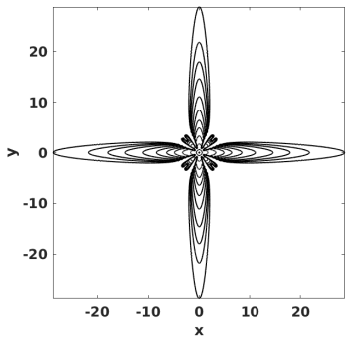

(b) Morphology of the precipitate

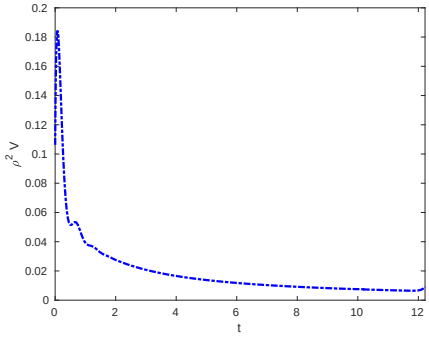

(c) Evolution of $\rho^2 V$ with time

FIGURE 4. Evolution of a precipitate under variable flux $J = 0.50(t + 1)$. The anisotropy parameter $\epsilon = 0.0067$. The initial shape is circular with radius $r = 0.10$. In (a), we plot the tip of the precipitate following Almgren's scaling law which in this case is $x \sim t^{1.4}$ and $y \sim t^{0.6}$. In (b), we plot the interfaces and in (c) we plot $\rho^2 V$ which becomes nearly flat as time progresses.

If we assume there exists a base shape $(x_0(s), y_0(s))$ such that the actual shape is given by

$$(t^{\alpha_1} x_0(s), t^{\alpha_2} y_0(s)), \tag{28}$$

then using Eq. (27) we obtain the relation $\alpha_1 + \alpha_2 = 2$, under the assumption that asymptotic shape looks like a *cross* described in [30]. We define $\rho = \frac{1}{\kappa}$, therefore

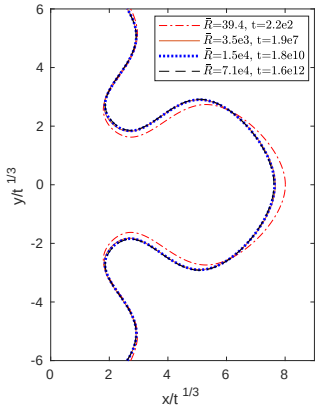

(a) Tip profile of the precipitate

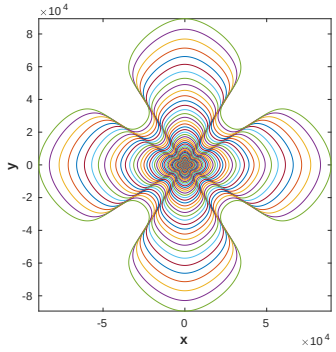

(b) Morphology of the precipitate

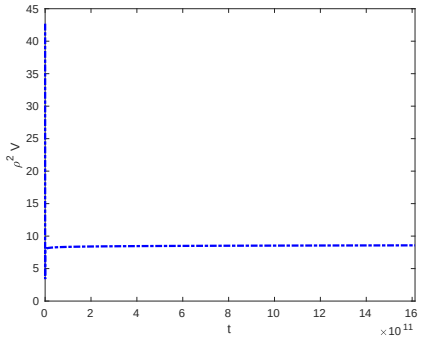

(c) Evolution of $\rho^2 V$ with time

FIGURE 5. Evolution of precipitate under rescaled flux $75/R$ and initial shape $r = 1 + 0.01\,(\cos 4\theta + \cos 5\theta)$ and anisotropy parameter $\epsilon = 0.01$. In the (a), we plot the tip of the precipitate following Almgren's scaling law which in this case is $x \sim t^{\frac{1}{3}}$ and $y \sim t^{\frac{1}{3}}$. In (b), we plot the interfaces and (c) we plot $\rho^2 V$, which remains flat after a brief transient period. Physical parameters of the simulation are same as in first shape of Fig. 3(a) in [25].

$\rho \sim \left(\frac{d^2x}{dy^2}\right)^{-1}$. Since $\dfrac{dx}{dt}\left(\dfrac{d^2x}{dy^2}\right)^{-2}$, the product of the tip velocity $\frac{dx}{dt}$ and ρ^2 should be time independent, we get $4\alpha_2 - \alpha_1 = 1$. This further results in

$$\alpha_1 = 7/5, \quad \alpha_2 = 3/5. \tag{29}$$

To verify the correctness of this analytic prediction, we ran a simulation with flux $J = 0.5(t+1)$ and $\epsilon = 0.0067$. In Fig. 4 we have displayed the results of simulation. The numerically computed shapes do exhibit the theoretically predicted scaling law at least between $\bar{R} = 105.64$ and $\bar{R} = 116.75$. The tips of the precipitate merge at these two time points.

In a short comment here we would like to mention that this type of simulation can also be expanded to include an exponentially increasing flux where $J \sim e^t$.

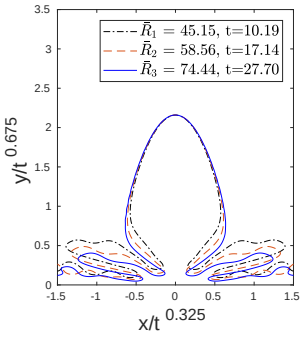

(a) scaling behavior of y-tip

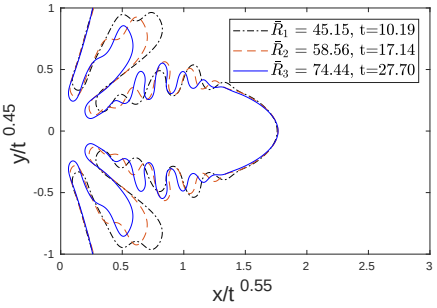

(b) scaling behavior of x-tip

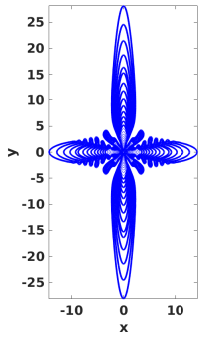

(c) Morphology of the precipitate

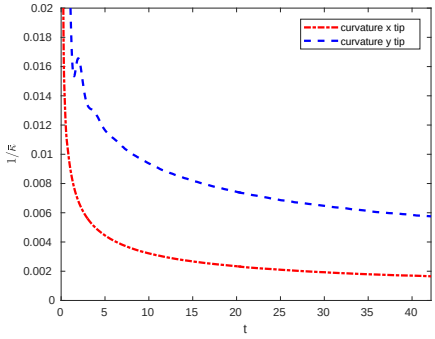

(d) Evolution of radius of curvature of tips along x and y-direction

FIGURE 6. Evolution of elastically stressed precipitate under uniaxial elastic field with flux $J = 1$. The elastic field has parameters $Z = 250$ and $\varepsilon^0_{11} = 0.01$. The precipitate grows under isotropic surface tension. The initial shape is circular with radius $r = 0.10$. The presence of uniaxial elastic field is evident by the shorter arm along the x-axis.

Then we should assume that the relation between base shape $(x_0(s), y_0(s))$ and the actual shape is given by

$$(e^{\alpha_1 t} x_0(s), e^{\alpha_2 t} y_0(s)) \tag{30}$$

and a calculation with ideas from previous subsection results in

$$\alpha_1 = 4/5, \quad \alpha_2 = 1/5. \tag{31}$$

3.3. Simulation results with time decreasing flux $J \sim \frac{1}{R}$. A very similar analysis as above, was carried out for the case with flux $J = \frac{c}{R}$ and $c = 75$. The reason for using this flux is that - after a transient period, the precipitate grows self-similarly in time (see [24, 25]). As shown in [25], for various values of constant c and various initial shapes, the precipitate evolves to different n-fold shapes. For example, the combination of $c = 75$ and a slightly perturbed circular precipitate with shape $r = 1 + 0.01\,(\cos 4\theta + \cos 5\theta)$ at $t = 0$ and anisotropy parameter $\epsilon = 0.01$

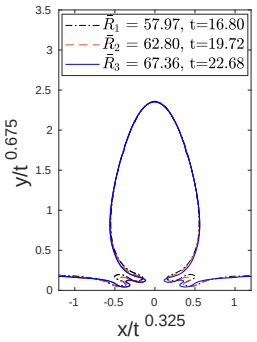

(a) scaling behavior of y-tip

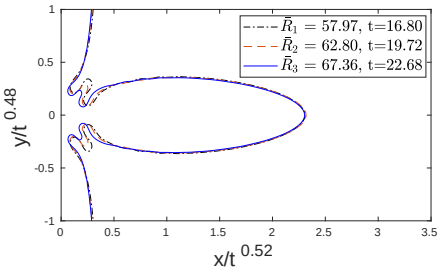

(b) scaling behavior of x-tip

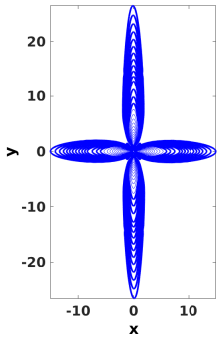

(c) Morphology of the precipitate

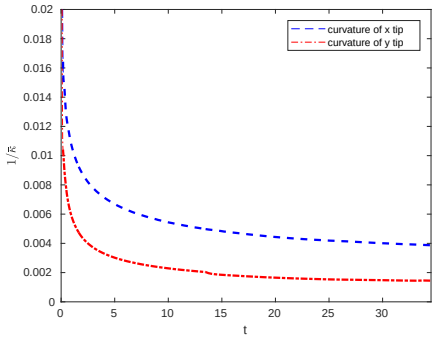

(d) Evolution of radius of curvature of tips along x and y-direction

FIGURE 7. Evolution of precipitate in presence of anisotropic surface tension and uniaxial elastic field. The strength of anisotropy is given by $\epsilon = 0.0067$ which is used in Almgren's Fig. (1). Rest of the parameters are same as those used to generate Fig. (6c). The presence of elastic field is marked by shorter arm along the x-axis.

results in a 4-fold shape (see Fig. (5a),(5b) and (5c)). In this case, the area of the precipitate changes as $t^{\frac{2}{3}}$ and therefore we found $\alpha_1 = \alpha_2 = \frac{1}{3}$. We plotted the tip profile with this scaling and found self-similarity. We observe that the contours between time $t = 2\times10^7$ to 1.6×10^{12} are indistinguishable under scaling. Therefore Almgren's law works the best in this case.

3.4. Asymptotic shape of the precipitate tip in presence of uniaxial elastic field. We perform a simulation where a precipitate was subjected to external uniaxial elastic field with $\varepsilon^0_{11} = 0.01$ and $\varepsilon^0_{ij} = 0$ otherwise, however, the surface tension that we applied is isotropic. We choose $\mu^P = 0.5, \mu^M = 1$ and $\nu^P = 0.2, \nu^M = 0.2$, where the superscript P/M denotes the precipitate/matrix. We set the parameter $Z = 250$. Other parameters remain the same as those used in the previous simulation. In Fig. 6, we display the result of simulation. The presence of the elastic field is evident from shorter precipitate arm along x-direction

as compared to y-direction. We fit the tip growth numerically and observe different scaling behavior for arms along x axis and y axis. While the x tip obeys the law $\alpha_1 = 0.55$ and $\alpha_2 = 0.45$, the y-tip seems to obey the law $\alpha_1 = 0.325$ and $\alpha_2 = 0.675$, at least in this phase of evolution.

In Fig. 7a and 7b, we display the evolution of an elastically stressed precipitate growing in presence of anisotropic surface tension with $\epsilon = 0.0067$ where we keep the other parameters unchanged from the previous case. The time corresponding to $\bar{R}_1$ is $t_1 = 10.19$, to $\bar{R}_2$ is $t_2 = 17.14$ and to $\bar{R}_3$ is $t_3 = 27.70$. Checking the self-similarity we find that the y tip obeys the same scaling law as the case with elastic field and isotropic surface tension, but the scaling behavior for the x tip changes slightly to $\alpha_1 = 0.52$ and $\alpha_2 = 0.48$. While the actual values of α_1 and α_2 might not be that important, we find a clear indication of self-similar tip growth in precipitates, with or without elasticity. That is one of the main findings of this work.

4. Conclusion and future work

In this paper, we have investigated the self-similar evolution of a dendritic precipitate driven by anisotropic surface tension and with or without elasticity. We observed that in the case of a pure diffusional growth, the Almgren's scaling law holds roughly true under constant flux and small anisotropy. In the case of strong of anisotropy, the law works for early time and not seem to work very well for long times. A different scaling law seems to hold for the cases of time dependent flux. We also performed numerical simulations of the dendritic growth of precipitates growing in an elastic media both under isotropic and anisotropic surface tension. While Almgren's law for growth comes from the analysis of the diffusion equations, the case of precipitate growth is more complex as one has to consider both elastic fields and diffusion effects. Therefore we performed numerical simulations. Our case studies suggest that scaling laws hold for precipitate growth problem but the laws are different from the one proposed for the diffusion only problem. As a future work we wish to study the effect of anisotropy on multiple precipitates.

5. Acknowledgements

S. L. acknowledges the support from the National Science Foundation, Division of Mathematical Sciences (NSF-DMS) grants DMS- 1720420. S.L is also partially supported by NSF, Division of Electrical, Communications and Cyber Systems grant, ECCS- 1927432. A. K. B. acknowledges partial support from the National Supercomputing Mission, `DST/NSM/R&D_Exascale/Sanction/2021/1` India.

References

[1] Li Q, Beckermann C. Scaling behavior of three-dimensional dendrites. Phys. Rev. E, 57(3):3176, 1998.

[2] Brener E, Temkin D. Noise-induced sidebranching in the three-dimensional nonaxisymmetric dendritic growth. Phys. Rev. E, 51(1):351, 1995.

[3] Greenbaum A, Greengard L, McFadden GB. Laplace equation and dirichlet-neuman map in multiply connected domains. J. Comput. Phys., 105:267, 1993.

[4] Ivantsov GP. Temperature field around a spherical, cylindrical, and needle-shaped crystal, growing in a pre-cooled melt. Doklady, Akademiya Nauk SSR, v. 58, 1947 p 567-569, 1947.

[5] Kessler DA, Levine H. Determining the wavelength of dendritic sidebranches. Europhys. Lett., 4(2):215, 1987.

[6] Langer JS, Müller-Krumbhaar H. Mode selection in a dendritelike nonlinear system. Phys. Rev. A, 27(1):499, 1983.

[7] Leo PH, Jou HJ. Shape evolution of an initially circular precipitate growing by diffusion in an applied stress field. Acta metall., 41(8):2271–2281, 1993.

[8] Qian XW, Cummins HZ. Dendritic sidebranching initiation by a localized heat pulse. Phys. Rev. Lett., 64(25):3038, 1990.
[9] Chen J-D. Radial viscous fingering patterns in hele-shaw cells. Experiments in fluids, 5(6):363–371, 1987.
[10] Bisang U, Bilgram JH. Shape of the tip and the formation of sidebranches of xenon dendrites. Phys. Rev. E, 54(5):5309, 1996.
[11] Barua A, Feng H, Li S, Li X, Lowengrub JL. An efficient rescaling algorithm for simulating the evolution of multiple elastically stressed precipitates. Commun. Comput. Phys., 14(4):940–959, 2013.
[12] Feng H, Barua A, Li S, Li X, Lowengrub JL. A parallel adaptive treecode for evolution of microstructure in elastic media. Commun. Comput. Phys., 15(2):365–387, 2014.
[13] Jou HJ, Leo PH, Lowengrub JS. Microsructural evolution in inhomogenous elastic media. J. Comput. Phys., 131:109, 1997.
[14] Langer JS. Dendritic sidebranching in the three-dimensional symmetric model in the presence of noise. Phys. Rev. A, 36(7):3350, 1987.
[15] Müller-Krumbhaar J, Langer JS. Sidebranching instabilities in a two-dimensional model of dendritic solidification. Acta Metall., 29(1):145–157, 1981.
[16] Pieters R, Langer JS. Noise-driven sidebranching in the boundary-layer model of dendritic solidification. Phys. Rev. Lett., 56(18):1948, 1986.
[17] Ignés-Mullol J, Maher JV. Experiments on anisotropic radial viscous fingering. Phys. Rev. E, 53(4):3788, 1996.
[18] Hou T, Lowengrub JS, Shelley M. Removing the stiffness from interfacial flows with surface tension. J. Comput. Phys., 114:312, 1994.
[19] LaCombe JC, Koss MB, Fradkov VE, Glicksman ME. Three-dimensional dendrite-tip morphology. Phys. Rev. E, 52(3):2778, 1995.
[20] Li S, Li X, Lowengrub JS, Glicksman ME. A deterministic mechanism for side-branching in dendritic growth. Tech Sci Press FDMP, 2(28):1–8, 2007.
[21] Nash GE, Glicksman ME. Capillarity-limited steady-state dendritic growthi. theoretical development. Acta Metall., 22(10):1283–1290, 1974.
[22] Nash GE, Glicksman ME. Capillarity-limited steady-state dendritic growthii. numerical results. Acta Metall., 22(10):1291–1299, 1974.
[23] Martin O, and Goldenfeld N. Origin of sidebranching in dendritic growth. Phys. Rev. A, 35(3):1382, 1987.
[24] Li S, Lowengrub JS, Fontana J, Palffy-Muhoray P. Control of viscous fingering patterns in a radial hele-shaw cell. Phys. Rev. Lett., 102:174501, 2009.
[25] Li S, Lowengrub JS, Leo PH. Nonlinear morphological control of growing crystals. Phys. D: Nonlinear Phenom., 208.3-4:209–219, 2005.
[26] Li S, Lowengrub JS, Leo PH. A rescaling scheme with application to the long time simulation of viscous fingering in a hele-shaw cell. J. Comput. Phys., 225:554, 2007.
[27] Glicksman ME, Lowengrub JS, Li S. Non-monotone temperature boundary conditions in dendritic growth. Proc. in Modelling of Casting, Welding and Adv. Solid. Processes XI, pages 521–528, 2006.
[28] Zhao M, Niroobakhsh Z, Lowengrub JS, Li S. Nonlinear limiting dynamics of a shrinking interface in a hele-shaw cell. J. Fluid Mech., 910, 2021.
[29] Zhao M, Ying W, Lowengrub JS, Li S. An efficient adaptive rescaling scheme for computing moving interface problems. Commun. Comput. Phys., 21(3):679–691, 2017.
[30] Almgren R, Dai WS, Hakim V. Scaling behavior in anisotropic hele-shaw flow. Phys. Rev. Lett., 71(21):3461, 1993.

Department of Mathematics, Indian Institute of Technology, Dharwad, Karnataka 580011, India
E-mail: abarua@iitdh.ac.in

Department of Applied Mathematics, Illinois Institute of Technology, Chicago, US 60616
E-mail: sli@math.iit.edu and lix@iit.edu

Department of Aerospace Engineering and Mechanics, University of Minnesota, Minneapolis, US 55455
E-mail: phleo@umn.edu